Biophysical Journal
Article

Biophysical Society

Unraveling VEALYL Amyloid Formation Using Advanced Vibrational Spectroscopy and Microscopy

Steven J. Roeters,[1,*] Mathias Sawall,[2] Carl E. Eskildsen,[3] Matthijs R. Panman,[1] Gergely Tordai,[1] Mike Koeman,[4] Klaus Neymeyr,[2,5] Jeroen Jansen,[4] Age K. Smilde,[6] and Sander Woutersen[1]

[1]Van't Hoff Institute for Molecular Sciences, University of Amsterdam, Amsterdam, the Netherlands; [2]Institut für Mathematik, Universität Rostock, Rostock, Germany; [3]Institute for Biodiversity and Ecosystem Dynamics, University of Amsterdam, Amsterdam, the Netherlands; [4]Institute for Molecules and Materials, Radboud University, Nijmegen, the Netherlands; [5]Leibniz-Institut für Katalyse, Rostock, Germany; and [6]Swammerdam Institute for Life Sciences, University of Amsterdam, Amsterdam, the Netherlands

ABSTRACT Intermediate species are hypothesized to play an important role in the toxicity of amyloid formation, a process associated with many diseases. This process can be monitored with conventional and two-dimensional infrared spectroscopy, vibrational circular dichroism, and optical and electron microscopy. Here, we present how combining these techniques provides insight into the aggregation of the hexapeptide VEALYL (Val-Glu-Ala-Leu-Tyr-Leu), the B-chain residue 12–17 segment of insulin that forms amyloid fibrils (intermolecularly hydrogen-bonded β-sheets) when the pH is lowered below 4. Under such circumstances, the aggregation commences after approximately an hour and continues to develop over a period of weeks. Singular value decompositions of one-dimensional and two-dimensional infrared spectroscopy spectra indicate that intermediate species are formed during the aggregation process. Multivariate curve resolution analyses of the one and two-dimensional infrared spectroscopy data show that the intermediates are more fibrillar and deprotonated than the monomers, whereas they are less ordered than the final fibrillar structure that is slowly formed from the intermediates. A comparison between the vibrational circular dichroism spectra and the scanning transmission electron microscopy and optical microscope images shows that the formation of mature fibrils of VEALYL correlates with the appearance of spherulites that are on the order of several micrometers, which give rise to a "giant" vibrational circular dichroism effect.

SIGNIFICANCE Amyloid aggregation by incorrectly folded proteins is associated with over 50 diseases in which (transient) oligomeric species are thought to play a particularly toxic role. Obtaining a detailed biophysical and structural understanding of such intermediate species is challenging with conventional techniques. Here, we present a combination of three vibrational spectroscopy techniques and two microscopy techniques (each sensitive to a different length scale), analyzed with novel multivariate curve resolution techniques that allow an unprecedented molecular view over length scales ranging from nano- to millimeters and timescales ranging from picoseconds to weeks. We apply the approach to reveal and characterize intermediates in the amyloid aggregation by the hexapeptide VEALYL, the most amyloidogenic segment of insulin.

INTRODUCTION

The formation of amyloid aggregated by incorrectly folded proteins is associated with over 50 diseases, including Alzheimer's and Parkinson's disease, Creutzfeldt-Jakob disease, prion diseases such as mad cow disease, Huntington's disease, and type II diabetes (1). Recently proposed "oligomer hypotheses," which state that intermediately formed oligomers and not mature fibrils, are the molecular species that are responsible for cell death, are gaining more and more evidence, for example, for Aβ (2,3) (related to

Submitted July 25, 2019, and accepted for publication May 11, 2020.

*Correspondence: s.j.roeters@chem.au.dk

Steven J. Roeters's present address is Kemisk Institut, Aarhus Universitet, 8000 C Aarhus, Denmark.

Matthijs R. Panman's present address is Department of Chemistry and Molecular Biology, University of Gothenburg, 40530 Gothenburg, Sweden.

Editor: Elsa Yan.

https://doi.org/10.1016/j.bpj.2020.05.026

Alzheimer's), α-synuclein (4,5) (related to Parkinson's), and islet amyloid polypeptide (6,7) (related to type-II diabetes). Monitoring the formation of amyloids from monomers through intermediates to mature fibrils is challenging with conventional techniques because they are not able to probe the many time- and length scales over which the process occurs. Here, we demonstrate how a combination of microscopy and vibrational spectroscopy techniques allows for a holistic comprehension of the amyloid formation process. We apply a combination of Fourier transform infrared spectroscopy (FTIR, also known as one-dimensional infrared spectroscopy (1D-IR)), nonlinear two-dimensional infrared spectroscopy (2D-IR), and vibrational circular dichroism (VCD) and perform optical microscopy and scanning transmission electron microscopy (STEM) to study the amyloid aggregation of the hexapeptide Val-Glu-Ala-Leu-Tyr-Leu (VEALYL). The three vibrational spectroscopy techniques complement each other because they are each sensitive to a different structural length scale. We focus on spectra of the amide-I band (1600–1700 cm^{-1}) because it is sensitive to the conformation of proteins. The combination of the omnipresence of the amide group in proteins (as peptide linkage between amino acids), and its large amide-I transition dipole moment, which leads to strong coupling between the local modes, results in unique spectral features across the bands that are sensitive to the tertiary structure and environment of proteins. In this frequency range, the IR frequencies are strongly influenced by the strengths of the hydrogen bonds the peptide groups engage in but also by the coupling between the amide-I modes (8). With 2D-IR, these couplings can specifically be determined, and one is more sensitive to structures that lead to large, delocalized normal modes (9), making the technique particularly suited to study amyloid fibrils (10–23). The technique has been applied previously to reveal the structure of intermediates formed in amyloid aggregation (24,25). VCD is, yet again, sensitive to even bigger structures because of the strong enhancement that can take place when the amyloid fibrils start to form bundles, twisting around each other (26–29). By combining these vibrational spectroscopy techniques with microscopy, we can correlate the vibrational spectra with morphology.

VEALYL, the hexapeptide segment of insulin that has the highest propensity for amyloid formation (30), is believed to play an important role in the aggregation of insulin (31,32). This 51-residue protein is an important glucose-uptake-mediating hormone, which is widely used to treat diabetes. When insulin aggregates during the manufacturing, purification, storage, or infusion, its activity is lost, which renders it therapeutically ineffective, and injected protein aggregates can even trigger an immune response (31).

A recent ion mobility mass spectrometry and gas-phase infrared spectroscopy study has provided insight into the structure of the early oligomers (up to nine monomers), revealing the presence of β-sheet structure in oligomers composed of more than three monomers, whereas smaller oligomers are composed of random coil structure (33). Amyloid VEALYL aggregates formed after 3 weeks of incubation have been studied in their crystalline form with x-ray crystallography (32) and in situ (in the incubation solution) form with NMR spectroscopy (34), revealing a nearly complete β-sheet conformation with little variation in the unit cell structure for various macromolecular polymorphs. The vibrational spectroscopy and microscopy methods employed here allow for an in situ and nondestructive investigation of VEALYL aggregation all the way from separate monomers to mature fibrils. By applying two multivariate curve resolution techniques (*FACPACK* and multivariate curve resolution (MCR) with alternating least squares (MCR-ALS)) to the recorded spectroscopic data, to our knowledge, new structural characteristics of the intermediate species are revealed.

MATERIALS AND METHODS

Sample preparation

VEALYL was bought in lyophilized form from GL Biochem (Shanghai, China). To exchange the protons present in the amide groups of the backbone of the peptide and to remove the remaining amount of trifluoroacetic acid that was used in solid-phase peptide synthesis, VEALYL was dissolved at a concentration of 18.5 mM in D_2O, after which 0.7 μL of 35 wt% DCl was added for each milliliter of solution (equivalent to a 0.084 M solution of DCl). The samples were then vortexed at 1400 revolutions per minute for 1 min to properly dissolve the peptides, after which the peptide solution was left to exchange ^1H for ^2H for 20 min. Subsequently, the samples were rapidly cooled to 77 K by immersion of the Eppendorf tubes in liquid nitrogen. After this, the samples were lyophilized by placing them in vacuum and freeze-drying for 8 h in a ScanVac Coolsafe (LaboGene, Alleroed, Denmark), in which 1 mL of peptide solution was fully lyophilized.

To minimize hydrogen exchange from the air with the sample, all subsequent steps were performed inside a glove box that is continuously flushed with N_2. The lyophilized VEALYL powder was resolvated in a solution containing 150 mM NaCl and 50 mM phosphate, leading to a pH of ~6. The aggregation was started according to the procedure described in (32): by lowering the pH to 2.5 with the addition of a few microliters of 1 M DCl. The solution was then vortexed at 1400 rpm for exactly 1 min. Subsequently, the pH was measured with a Thermo Scientific Orion 2-Star Plus pH Meter (Thermo Fisher Scientific, Waltham, MA). Unless noted differently, a VEALYL concentration of 11 mM was used.

1D- and 2D-IR and VCD spectroscopy

A Bruker Vertex 70 FTIR spectrometer (Bruker, Billerica, MA) is used to measure the 1D-IR (FTIR) spectra of 5-μL drops of sample solution in between two CaF_2 windows. A greased 50-μm spacer prevents the two CaF_2 windows from touching each other and seals the sample solution to prevent atmospheric water vapor from changing the H/D ratio. The FTIR data presented in Fig. 1 are normalized on the integrated area of the amide-I region (1600–1700 cm); without this normalization step, the effect of the slow acidic hydrolysis of the peptide bonds is even more pronounced.

The setup used to measure the 2D-IR spectra has been described in detail before (35). In short, we generate 1 kHz of 3 mJ pulses with a central wavelength of 794 nm and convert this in an optical parametric amplifier into mid-IR (~20 μJ, ~6100 nm) that has a spectral full width at half max (FWHM) of 150 cm^{-1}. The beam is then split into a probe and reference beam (each 5%), and a pump beam (90%) that is aligned through a Fabry-Pérot interferometer.

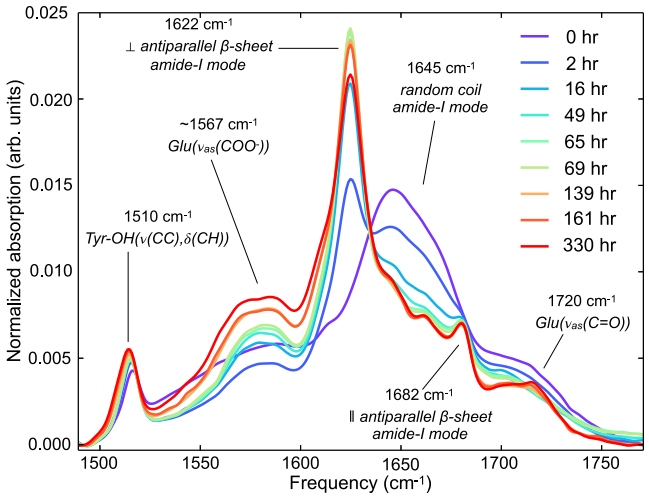

FIGURE 1 1D-IR (FTIR) spectra of 11 mM VEALYL solution after the pH is lowered from 7 to 2.5. The spectra are first background subtracted with a buffer-only spectrum and then normalized with respect to the amide-I area of the first spectrum. The decreasing, broad ~1645 cm^{-1} peak indicates decreasing amounts of random coil structures, which are transformed into intermolecular β-sheets, as indicated by the increasing peaks at ~1622 and ~1682 cm^{-1}. To see this figure in color, go online.

Subsequently, the pump beam is narrowed to a FWHM of 10 cm^{-1}. The pump and probe beams are overlapped in the sample with a 1.5-ps delay in an ~250-μm focus. The signal (Δabsorption (α)) is recorded after dispersion by an Oriel MS260i spectrograph (Newport, Irvine, CA) onto a 32-pixel mercury cadmium telluride (MCT) array with a resolution of 3.9 cm^{-1}. The background is subtracted by comparing the $\Delta\alpha$ at $(t_{probe} - t_{pump}) = 1.5$ and -10 ps. The spectra were measured at room temperature, and all presented 2DIR spectra are measured with a perpendicular orientation of the pump versus probe beam. To avoid beam-pointing differences for the two polarizations, we recorded the spectra by rotating the probe beam in a 45° angle with respect to the pump beam and selecting the probe beam component that is either perpendicular or parallel to the pump beam using a polarizer after the sample. To minimize scattering contributions, we measured the average of two photoelastic modulator (PEM)-induced pump delays, such that the interference between the scattered pump beam and the probe beam has a 180° phase in one delay with respect to the other delay (analogous to the scatter reduction presented in (36) in which a wobbler is used for the same purpose).

The VCD spectra are also measured with a Bruker Vertex 70 FTIR spectrometer, using the PMA 50 Polarization Modulation Accessory (Bruker). The time trace in Fig. 7 is constructed by first correcting for an overall offset by subtracting the average intensity of the 1330–1365 cm^{-1} range and subsequently taking the average of the absolute signal strengths at 1621 and 1636 cm^{-1} (the spectrum's maximum and minimum, respectively). The spectra were recorded by averaging for 10 min.

Optical microscopy

The optical micrographs of VEALYL are captured of the IR cell of the sample in between two IR cell (CaF_2) windows using a Leica DM-IRB microscope (Leica, Wetzlar, Germany) and a Pixelink USB-camera (Pixelink, Ottawa, Ontario, Canada). Phase contrasting is used for the images and a 50× magnification.

STEM

The STEM sample preparation was performed by adsorbing a 1.5-μL drop of VEALYL solution on a carbon-coated grid with a 300-μm mesh size (Ted Pella, Redding, CA) for 5 min. Excess liquid was removed by pipetting once and is exchanged for 1.5 μL of pH-2.0 Milli-Q water (Millipore-Sigma, Darmstadt, Germany). The grid was air-dried at 37°C and then transferred under vacuum into the STEM setup. Before recording the bright-field STEM micrographs, condenser stigmators were adjusted to give a circular beam profile, and the beam was carefully centered and spread to produce uniform illumination over the field of view. The micrographs were acquired using an FEI Verios 460 microscope (FEI, Hillsboro, OR) operating at 20-kV-electron beam energy and 50-pA current.

RESULTS AND DISCUSSION

General observations

As in previous studies of amyloid formation by VEALYL (30,32,34), we trigger the aggregation by lowering the pH to 2.5, which protonates the sidechain of the glutamic acid residue (pKa = 4.15), thereby removing its negative charge. Lowering the pH greatly enhances the amyloid fibril formation by VEALYL (30,32). In Fig. 7, an overview is presented of the results of the five experimental techniques employed to monitor the amyloid aggregation of an 11-mM VEALYL solution after lowering the pH. The first sign of amyloid aggregation are the β-sheet peaks in the 1D-IR and 2DIR spectra that are observed after a lag phase (37) of 30 min to 3 h (this variation was observed within five repeated experiments) of incubation at a VEALYL concentration of 11 mM, whereas at neutral pH, the amide-I spectrum remains unchanged with respect to the monomeric random coil spectrum, even after 3 months. We find that increasing VEALYL concentration (with a minimum concentration of 2 mM), temperature, and agitation decreases the aggregation lag time, which is in line with observations of other amyloidogenic proteins (38–41). The fibrils formed at pH 2.5 can be dissolved by raising the pH of the aggregating solution above the pK_a of Glu (see Fig. S1). The formed fibrils are very stable at pH 2.5, as evinced by the fact that they could not be melted with temperature, as opposed to the fibrils formed by various other hexameric peptides.

Early aggregation: intermediate structures observed with time-dependent 1D- and 2D-IR spectroscopy

1D-IR (FTIR) spectroscopy

Time-dependent 1D-IR spectra of the amide-I and adjecent sidechain-absorption region (Fig. 1) show a conformational transition after the pH is lowered from 7 to 2.5 at t = −5 min (these 5 min are required to prepare the IR sample and to completely purge the sample chamber of the IR spectrometer from atmospheric water vapor). After a lag phase of 30 min, the peptides aggregate during a growth phase of ~1000 min into mature fibrils that are mainly present during the final plateau regime that is subsequently reached.

The largest change is observed in the amide-I band, where a single broad peak centered at ~1645 cm^{-1} transforms into

an intense peak at ~1622 cm^{-1} and a small peak at ~1682 cm^{-1}. This change indicates a molecular transition from random coil to amyloid structure (42). The sidechain absorptions of Tyr-OD (ν(CC), δ(CH)) and deprotonated and protonated Glu (ν_{as}(COO-) and ν(C=O)) are visible at ~1515, ~1575, and ~1720 cm^{-1}, respectively (8). The fact that the frequency of the Glu (ν(C=O)) sidechain vibration is higher than 1706 cm^{-1} indicates that the C=O is not fully hydrogen bonded (43), which can be expected in the dry steric-zipper (32) environment inside the fibril core (Fig. S2). The intensities (normalized to the total amide-I area) of the β-sheet peaks reach a maximum at ~70 h, after which they decrease again (see also *fifth row* of Fig. 7). We ascribe this decrease to slow acidic hydrolysis of the peptide bonds. As a result of this process, the pH increases, which leads to a partial back conversion of amyloid to random coil structure (Fig. S1).

Singular value decomposition analysis. To estimate how many spectroscopic species are present in the data, we first perform a singular value decomposition (44) (SVD; see Fig. 2). When such an analysis is applied to a time-dependent spectral data set, the data are decomposed in orthogonal spectral and temporal profiles, and the singular value of each component indicates how much the component contributes to the total data set.

An SVD is a factorization of the two-dimensional data set D of the following form:

$$D = U\Sigma V^T = \sum_{i=1}^{\min(m,n)} u_i \sigma_i v_i^T,$$

where the columns of $U(m \times m)$ are the left singular vectors of D, Σ $(m \times n)$ is a diagonal matrix containing the singular values σ_i on its diagonal in a decreasing order, and the columns of $V(n \times n)$ are the right singular vectors. Both U and V are orthonormal. Moreover, u_i is the ith column of U and hence the ith left singular vector of D. Analogically, v_i is the ith column of V and hence the ith right singular vector of U. The singular values can be viewed as weights and are multiplied with the left and right singular vectors when estimating D. A large singular value indicates that the corresponding singular vectors carry systematic information, whereas a small singular value indicates that the corresponding singular vectors carry noise.

In the SVD of the time-dependent 1D-IR data of aggregating VEALYL (with $m = 417$ time points and $n = 300$ frequencies) presented in Fig. 2, the left singular vectors describe the temporal profiles, and the right singular vectors describe the spectral profiles of the species. Before the SVD, D was column-wise mean-centered. The first three singular values are clearly larger than the remaining singular values. Therefore, it appears that with 1D-IR spectroscopy, only three species can be resolved in the amyloid aggregation process of VEALYL. The right singular vector of the fourth component especially shows that this component mostly contains experimental noise that cannot be attributed to absorptive features of the protein.

Because of the fact that both U and V are orthonormal, an SVD provides a unique solution. However, this orthogonality constraint causes the left and right singular vectors to not, respectively, resample the pure temporal and spectral profiles of the physical species.

Determination of the rotational ambiguity with FACPACK. To determine the concentration and spectral profiles of physical species that give rise to a time-dependent spectral data set, MCR techniques can be applied. However, such techniques suffer from the so-called rotational ambiguity of the solution. This means that, in general, a factorization is not unique, and a continuous range of possible factorizations exists. In other words, there are many different linear combinations of temporal and spectral profiles that can reproduce the experimental data. In this respect, non-SVD decompositions differ from an SVD decomposition; because of orthogonality between the singular vectors, an SVD decomposition gives only one unique

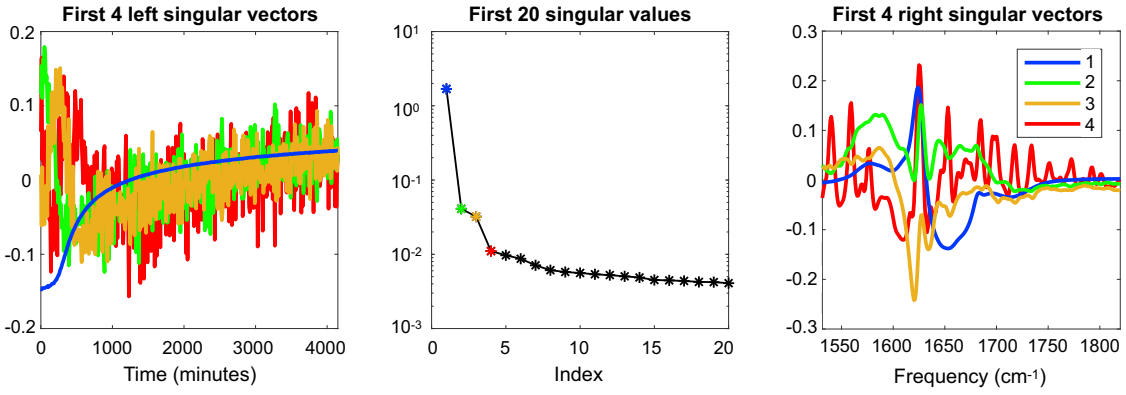

FIGURE 2 SVD analysis of the time-dependent FTIR spectra of aggregating VEALYL. For the first four components, the left- and right-singular vectors are depicted in blue, green, orange, and red, respectively. To aid the analysis, a spectrum measured at $t = 5250$ min (data not shown) was included in the data set to include a time point at which the aggregation process was fully completed. To see this figure in color, go online.

decomposition. Due to the orthogonality constraint, SVD decompositions do not provide a "proper" pure component decomposition, and return temporal and spectral profiles with negative entries. To reconstruct all possible concentration and spectral (absorption) profiles, $\boldsymbol{C}$ and $\boldsymbol{A}$, respectively, of the pure components, the first s components of a truncated SVD are transformed such that both $\boldsymbol{C}$ and $\boldsymbol{A}$ only contain nonnegative entries (45). Using the software package *FACPACK* (46,47) the area of feasible solutions (AFS; see e.g., (48–53)) is determined according to

$$\boldsymbol{D} = \underbrace{\boldsymbol{U}\cdot\boldsymbol{\Sigma}\cdot\boldsymbol{T}^{-1}}_{\boldsymbol{C}}\cdot\underbrace{\boldsymbol{T}\cdot\boldsymbol{V}^{T}}_{\boldsymbol{A}}, \tag{1}$$

with $\boldsymbol{U}\in\mathbb{R}^{m\times s}$, $\boldsymbol{\Sigma}\in\mathbb{R}^{s\times s}$, and $\boldsymbol{V}\in\mathbb{R}^{n\times s}$ as the truncated factors of the SVD and $\boldsymbol{T}\in\mathbb{R}^{s\times s}$ as the transformation matrix that completely represents all possible nonnegative concentration and spectral profiles ($\boldsymbol{C}\in\mathbb{R}^{m\times s}$ and $\boldsymbol{A}\in\mathbb{R}^{s\times n}$, respectively), where $\boldsymbol{D}=\boldsymbol{CA}$ follows from the Lambert-Beer law (the AFS computation is explained in detail in the Supporting Materials and Methods). The AFS sets cover all possible (concentration and spectral) profiles that can be part of an MCR solution.

Based on the SVD analysis, we assume that there are three components with different absorption spectra in the calculation of the AFS. The data set might include contributions from more species, but because of the noise and linear dependencies between the components, it is only possible to identify three linearly independent components. Hence, we compute decompositions of $\boldsymbol{D}$ with respect to three components ($\boldsymbol{C}$ is an $m\times 3$ matrix and $\boldsymbol{A}$ is a $3\times n$ matrix). Furthermore, we compute the AFS also with respect to three components.

The resulting feasible profiles are shown in Fig. 3, and the AFS sets are shown in Fig. S3. With the applied constraints (nonnegativity for both the spectral and temporal profiles) and a tolerance for negative entries of 0.0086 OD, there is a range of feasible spectra and associated concentration profiles (time dependencies) that are all equally compatible with the experimental data. The spectral shapes of all of the possible intermediate species indicate that with time, the amount of β-sheet increases, and the amount of random coil structure decreases. The sidechain ν_{as}(COO-) and ν(C=O) peaks show that the Glu residues of the intermediates (*green curves*) are more deprotonated than the Glu residues of the monomers. The presence of deprotonated Glu residues in the amyloid aggregates formed by VEALYL under these experimental conditions has been observed before in NMR experiments (34). This deprotonation might be due to a lower pK_a of the Glu sidechain in the fibrillar structure: the formation of a hydrogen bond between deprotonated Glu side chains and theNH_3^+ (Val) terminus of the peptide stabilizes the carboxylate ion form of Glu (54,55). Alternatively, the aforementioned pH increase due to the slow acidic hydrolysis of peptide bonds could explain the deprotonation of the Glu side chains in the more mature intermediates.

MCR-ALS analysis. Similar solutions are found when an MCR-ALS analysis is performed (56,57). With this method, the physical components that give rise to the variations measured in the experiment are determined in a different manner: the data are fitted while various constraints and assumptions are applied (58) (see Supporting Materials and Methods for the computational methods).

By performing an MCR-ALS analysis on the 1530–1800 cm^{-1} data assuming nonnegative temporal and spectral profiles, we find evidence for the appearance and disappearance of intermediate species during the aggregation process, similar to the FACPACK analysis (see Fig. S4–S6). The intermediate spectra obtained with the MCR-ALS analysis reflect structures that are more fibrillar and deprotonated than the monomeric species.

2D-IR spectroscopy

2D-IR spectroscopy of the amide-I region is a very sensitive tool to study the secondary structure of (aggregating) proteins (9). The spectra are recorded by exciting the protein solution at a specific frequency ν_{pump} and probing the resulting changes in the absorption over the entire IR frequency range. Scanning ν_{pump} and plotting the absorption change as a function of ν_{pump} and ν_{probe}, one can obtain 2D-IR spectra that can be regarded as the vibrational analog of 2D-NMR spectra. When two normal modes A and B are coupled, exciting mode A ($\nu_{pump}=\nu_A$) causes an absorption change at the frequency of mode B ($\nu_{probe}=\nu_B$) and vice versa, and this gives rise to crosspeak patterns in the 2D-IR spectrum. 2D-IR spectroscopy is particularly suited to study the formation of amyloid fibrils (9–25) Because delocalized vibrational eigenmodes—which are abundant in amyloid fibrils—give a stronger 2D-IR signal than localized eigenmodes, the 2D-IR spectrum can provide additional structural insight that cannot be deduced from the 1D-IR (FTIR) spectrum, crosspeaks between eigenmodes give additional information on the fibril structure, and the shape of the peaks also gives additional information about the heterogeneity of the fibril structure (21), also through the anisotropy $R=\left(\Delta A_{par}-\Delta A_{perp}\right)/\left(\Delta A_{par}+2\Delta A_{perp}\right)$, with $\Delta A_{par,\ perp}$ as the crosspeak intensity for parallel and perpendicular pump versus probe polarization, from which the relative orientation of the associated modes can be derived with $R=(3\cos(\theta)^2-1)/5$ (9).

As expected, the transition from a broad distribution of random coil modes centered around 1645 cm^{-1} into two sharp amyloid β-sheet modes at ~1622 and ~1682 in (mature) fibrils (Fig. 1) is also visible in the 2D-IR spectra (Fig. 4). The anisotropy of the crosspeak at $(\nu_{probe},\nu_{pump})=(1682,1622)$ cm^{-1} is $R=-0.21\pm0.03$, indicating that there is a $90\pm11^\circ$ angle between the modes that the 1622 and the 1682 cm^{-1} peaks are composed of, which is consistent with the assignment of the modes to the

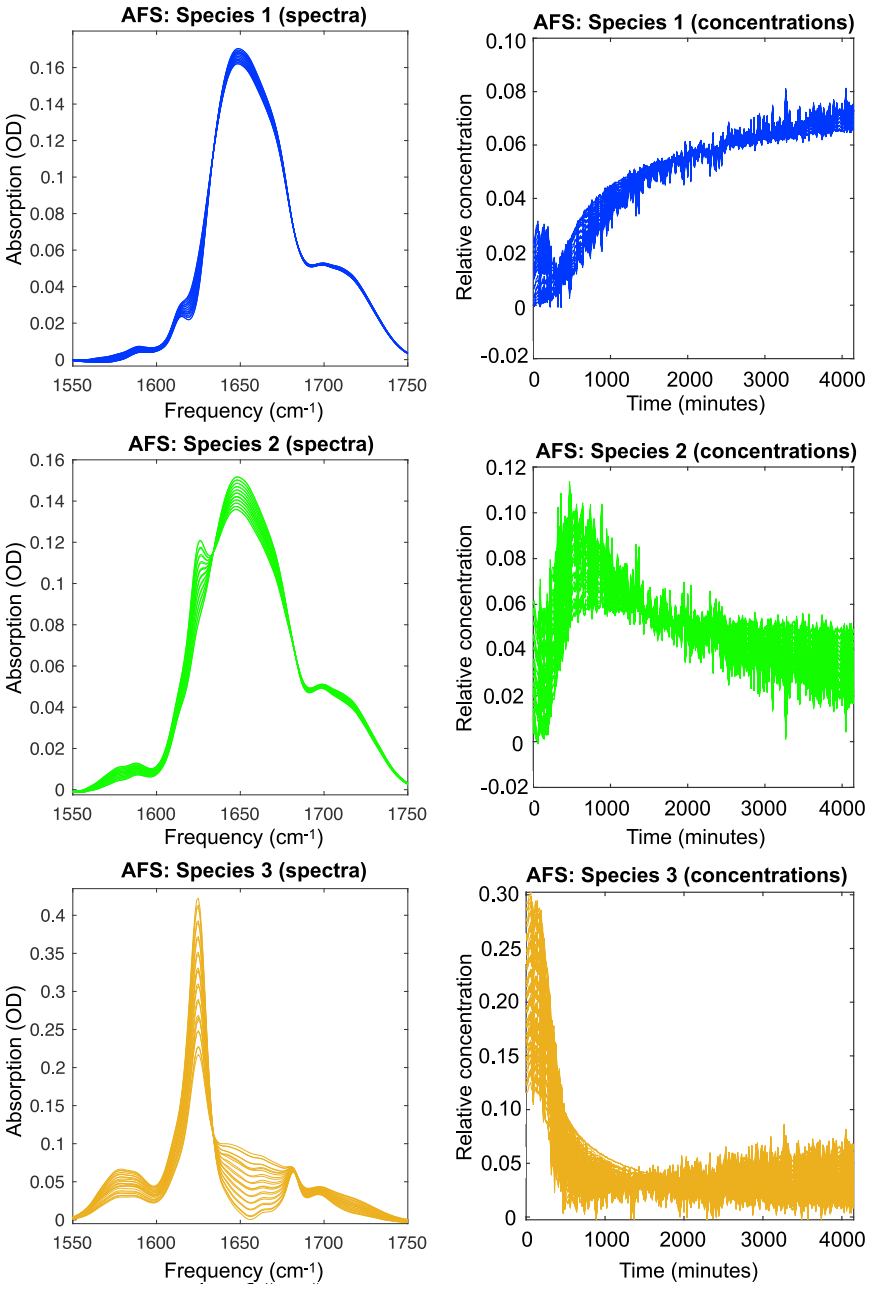

FIGURE 3 Feasible spectra (*left column*) and associated concentration profiles (*right column*). To see this figure in color, go online.

$\nu_{\perp}$ and $\nu_{\parallel}$ of an antiparallel β-sheet (59,60). This angle is reproduced with one-exciton spectral calculations (9,23) based on the crystal structure of the amyloid fibrils formed by VEALYL (Protein Data Bank, PDB: 2OMQ), by which the 2D-IR spectrum can also be reproduced well (see Fig. S7), indicating that the structures formed at the end of the aggregation experiment are similar to those obtained by Ivanova et al. (30).

Also, the ratio of the 1D-IR/2D-IR spectrum can be used to determine the magnitude of the transition dipole moment of a given isolated mode (61). However, for amyloids, the vibrational modes extend over at least a dozen strands, which approaches the asymptotic number of strands after which the delocalization no longer influences the β-sheet absorption (20), thereby limiting the discriminating ability of the transition dipole strength determination. Subtle variations in interlocal mode differences and dihedral angles that are present in the fibril structure lead to a distribution of couplings whose average value determines the exact frequency of the $\nu_{\perp}$ β-sheet mode. Lomont and co-workers (20) ascribe the fact that they measured a variation >2 in the transition dipole moment magnitude to variations in the couplings. Because of the difficulty of reproducing the transition dipole magnitudes in heterogeneous amyloid samples, which we also

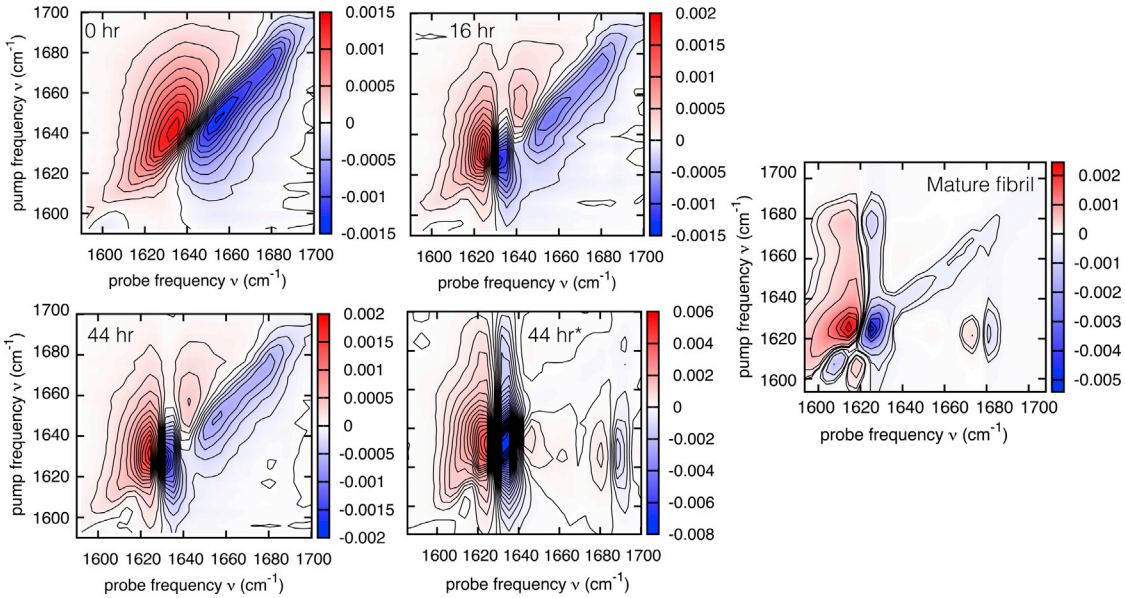

FIGURE 4 2D-IR spectra of VEALYL after the pH of the solution has been lowered from 7 to 2.5. The increasing signal strength at ~1622 and 1682 cm^{-1} indicates that amyloid β-sheets are formed, and the decreasing inverted slope of the modes with time indicates that the heterogeneity is decreasing. The spectrum labeled "44 h*" is measured at a spot in the IR sample cell ~500 μm away from the four preceding spectra (all of a 11.75 mM VEALYL sample). The mature fibril is measured of a 26.5 mM solution that was incubated for 5 days. We did not observe a strong dependency of the spectral line shape once the concentration threshold for aggregation was exceeded. To see this figure in color, go online.

observed in previous measurements in our laboratory of the transition dipole moment of the low-frequency β-sheet mode of α-synuclein (unpublished data), we did not determine them here for VEALYL. The procedure we follow here to prepare the amyloid VEALYL samples (i.e., lowering the pH right before pipetting the sample volume into an IR cell) results in a sample heterogeneity that affects time-dependent measurements of VEALYL aggregation with 2D-IR spectroscopy. Because the overlap of the focused pump and probe beam is typically of the order of 250 μm, there is a certain probability that the beams are not focused at a nucleation site (see Fig. 7 for an estimate of the typical sizes of the aggregates in the different aggregation phases), as can be seen by comparing the lower two spectra in Fig. 4 that have been recorded 500 μm from each other, which contain different amounts of random coil and amyloid β-sheet structure.

The line shape of the 2D-IR peaks shows that there is a large spectral inhomogeneity, as indicated by the inverted slope of the line through the zero crossings. A small (close to 0), inverted slope through these points indicates a mode with a small spectral inhomogeneity, whereas an inverted slope close to unity indicates a large spectral inhomogeneity (62–64). When the VEALYL molecules are in their monomeric state, the inverted slope is close to unity; with increasing aggregation, the inverted slope becomes smaller, indicating a more homogeneous structure, as can be expected for the amyloid crystals that are formed.

An SVD analysis of the combined 2D-IR data set presented in Fig. 4 in its unrolled, or flattened, 122 (time points) × 1024 (frequency points) form (see Fig. S8) also shows that there are three components that describe absorptive features of the protein, whereas other components describe noise contributions (see Fig. S9), corroborating the conclusions derived from the SVD analysis on the 1D-IR data set.

Advanced aggregation: STEM and optical microscopy and VCD spectroscopy reveal that the appearance of higher-order structures correlates with the presence of mature fibril structures

VCD spectroscopy

VCD measures the difference in absorbance of left- and right-handed circularly polarized light (65,66). When applied to the amide-I region, the chiral properties of proteins can be probed. Time-dependent VCD spectra of aggregating VEALYL show maxima at 1567 and 1621 cm^{-1} and minima at 1462, 1510, 1635 (with a shoulder at 1649), 1678, and 1710 cm^{-1}, which all grow with time (see Fig. 5). We assign these peaks to ν_{as}(COO-) modes of deprotonated Glu residues, amide-I modes of amyloid β-sheets, ν_s(COO-) modes of deprotonated Glu residues, (ν(CC), δ(CH)) modes of Tyr-OH residues, other amide-I modes of amyloid β-sheets, and to ν_{as}(C=O) of protonated Glu residues, respectively. Interestingly, the amide-I VCD spectra of VEALYL fibrils are "reverse fibril" spectra, which are nearly mirror images with respect to the canonical "normal fibril" spectra published by Kurouski et al. for insulin at the same pH (~2.5) (28,29,67). The reversed VCD

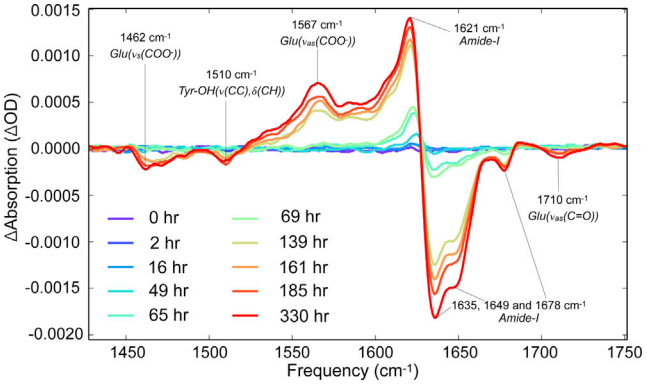

FIGURE 5 VCD spectra of 11 mM VEALYL after the pH of the solution has been lowered from 7 to 2.5, with tentative assignments indicated. The increasing signal strength at ~1621 and 1635 cm^{-1} indicates that chiral structures are formed that are of the order of 6 μm (the wavelength equivalent of ~1650 cm^{-1}). To see this figure in color, go online.

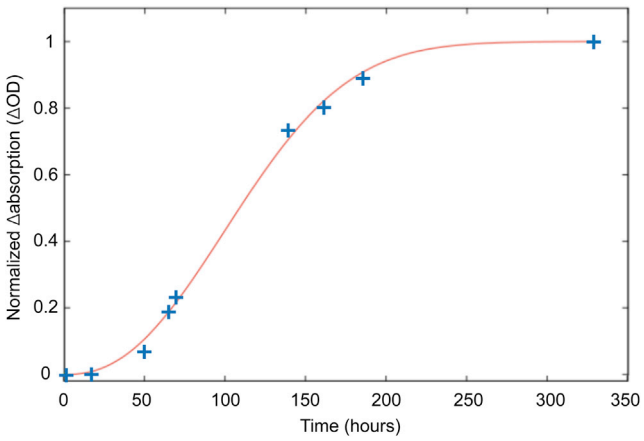

FIGURE 6 The maximum amplitude of the VCD signal at 1622 cm^{-1} versus time, fitted with the standard Avrami equation with $n = 2.5$. To see this figure in color, go online.

spectrum of VEALYL compared to the VCD spectrum of full-length insulin fibrils indicates a difference in β-sheet conformation and/or stacking geometry. The evidence presented in (29) indicates that differences in the supramolecular organization of filaments are the principal underlying cause of reversed VCD spectra of amyloid fibrils. The lack of an observable twist in the STEM images (see Figs. 7 and S10) is consistent with this explanation, although only large-diameter twists would be observable with this technique. But besides a difference in the supramolecular organization, the origin of the phase reversal may also lie in the different β-sheet conformation, which is thought to differ considerably between VEALYL (32) and insulin (68).

The VCD signal still grows by a factor of ~7 after $t >$ 50 h, whereas the shape of the 1D-IR spectra hardly changes from this point onwards. This indicates that the VCD intensity is not determined by structural features at the nanometer scale (as these would also affect the 1D-IR spectra).

Optical and electron microscopy

On the other hand, the light and electron microscopy images (see Figs. 7 and S10) do reveal a large conformational change that occurs from this time point onwards: the appearance of higher-order aggregates known as "spherulites" (69,70). This makes it likely that the observed "giant" VCD effect (29,71,72) is caused by the appearance of chiral aggregates that are of the order of the wavelength of the probe light, possibly due to a resonance effect. The twist of in silico VEALYL fibrils observed in molecular dynamics simulations in which the crystal structure that was resolved in ref. (32) was relaxed (34) may also contribute to the strong VCD signal.

Additionally, the STEM images reveal the appearance of curved structures after 2 h of incubation, which are probably protofibrils: intermediate structures that already have some fibrillar features but are not yet crystalline. Given the coexistence of these structures with the intermediate species observed in the 1D-IR data (see Fig. 7), these are probably composed partly of random coil structure and partly of intermolecular β-sheet.

An SVD and MCR-ALS analysis of the time-dependent VCD spectra of aggregating VEALYL (data not shown) shows that only a single component is present in the data set. The data can be fitted well with the Avrami equation, which describes crystallization in three dimensions (73–75):

$$f(t) = \frac{I_\infty - I(t)}{I_\infty - I_0} = 1 - e^{-kt^n}, \qquad (2)$$

where $f(t)$ is the fraction of crystallized material, I_∞ is the asymptotic VCD intensity at infinite time, $I(t)$ is the time-dependent VCD intensity, I_0 is the intensity at $t = 0$, k is a constant containing only time-independent factors, and the integer exponent n yields information about the mode of nucleation and the shape of the developing structures (76), with $n = 1$ indicating a needle-like growth, $n = 2$ indicating a disk-like growth, $n = 3$ indicating a sphere-like growth, and $n = 4$ indicating three dimensions of growth and a constant nucleation rate (77). The fact that the data are fitted well with the noninteger value of $n = 2.5$ (see Fig. 6) indicates a dimensionality that is in between disk-like and sphere-like growth, which is consitent with the STEM images (Fig. 7 and Fig. S10). However, interpretation of the Avrami constant is difficult; there have been almost as many cases in which n did match the observed crystal growth as when it did not (78).

CONCLUSIONS

By combining three vibrational spectroscopy techniques with two microscopy techniques, the aggregation of

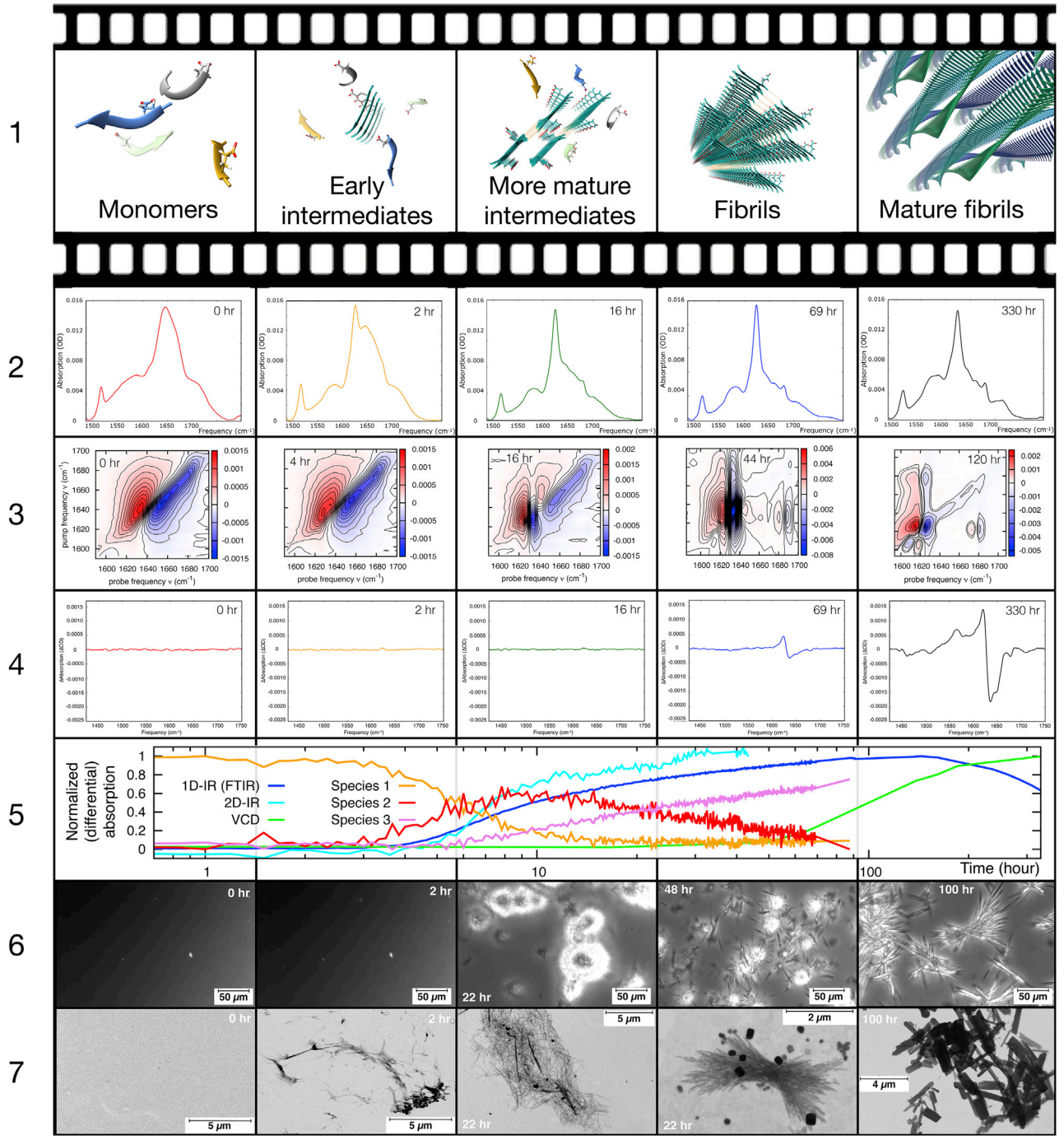

FIGURE 7 An overview of the data, analysis, and interpretation of the vibrational spectroscopy and imaging techniques used to study the amyloid formation of VEALYL. Row 1 shows the qualitative description and artist impressions of the structural interpretations of the various aggregation phases. Row 2 shows the 1D-IR (FTIR) spectra. Row 3 shows the 2D-IR spectra. Row 4 shows the VCD spectra. Row 5 shows the normalized profiles of the intensity at VEALYL's amyloid β-sheet frequency (1622 cm^{-1}) for the various techniques and concentration profiles of the three species from the FACPACK analysis of the 1D-IR data. Row 6 shows the light microscope images. Row 7 shows the STEM images. The 2D-IR spectra were recorded only up to 44 h of the same sample due to experimental procedural reasons (see main text). The third and fourth STEM images are recorded of the same sample with a VCD intensity that is 50% of the maximum, and an amyloid β-sheet IR signal that is already at its maximum because the different species (as shown in the *fifth row*) coexist when the intermediates and the mature fibrils are formed. To see this figure in color, go online.

VEALYL can be monitored from solvated monomers to intermediates and to insoluble mature fibrils. In Fig. 7, we give an overview of the different stages of this process, as observed in our experiments. The figure shows that each technique is sensitive to a specific range of length scales. By applying this combination of methods to other, potentially more complex, amyloid formation processes, detailed descriptions of the mechanism of the formation could be obtained. In the case of the amyloid aggregation of VEALYL, there appears to be limited structural variation among the observed molecular species that play a role in the amyloid aggregation process; they are composed of random coil structure and antiparallel β-sheets with an increasing amount of β-sheet structure with increasing aggregation. This is in line with previous ion mobility-spectrometry-mass spectrometry and gas-phase infrared spectroscopy observations for VEALYL (33). The molecular sensitivity of the vibrational techniques has now revealed that there are differences in the protonation state of the different molecular species that play a role in the aggregation. Also, the eventual observation of homogeneous and bundled fibrils, as indicated by the 2D-IR line shape and the VCD intensity, respectively, is in line with previous studies (32,34). By using the here-employed vibrational spectroscopy techniques to observe the transformation of monomers to oligomers and finally to mature fibrils in an in situ manner, we can continuously monitor the molecular evolution.

We show how MCR analyses of 1D- and 2D-IR amide-I spectra of amyloid proteins can provide insight into the mechanism of molecular processes. In the case of the amyloid aggregation of VEALYL, the analysis revealed intermediate species with an increased deprotonation state and an increased intermolecularly hydrogenbonded β-sheet structure, even though the exact spectrum is subject to rotational ambiguity. It should be noted that the spectrum of the intermediate species (depicted in Fig. 3) could reflect a group of species in a continuum of intermediate species that share certain distinct spectral features, or a group of relatively stable intermediates in a continuum of incrementally growing aggregates.

When vibrational spectra are complemented by spectral calculations (9,71), e.g., on molecular structures obtained with molecular dynamics simulations, more detailed structural information can be derived. Also, the application of advanced analysis methods on the time-dependent 2D-IR data (like parallel factor analysis (PARAFAC) or Tucker modeling techniques that have been developed especially for three-dimensional data sets) could allow an even more detailed analysis of amyloid systems (79).

For amyloid systems whose aggregation cannot be triggered like that of VEALYL, a large variation in the so-called "lag phase" might hinder connecting the results from the different techniques straightforwardly. However, in that case, an internal calibration of the different spectroscopic measurements can be obtained by deriving the 1D-IR spectrum from the 2D-IR and VCD spectra, as has been done in Fig. S11 for the data presented in this article.

Overall, we present a, to our knowledge, novel combination of techniques to study amyloid formation and show that many structural details can thus be revealed on length scales ranging from nano- to millimeters and timescales ranging from picoseconds to weeks.

SUPPORTING MATERIAL

Supporting Material can be found online at https://doi.org/10.1016/j.bpj.2020.05.026.

AUTHOR CONTRIBUTIONS

S.J.R. and S.W. designed the research. S.J.R., M.P., and G.T. carried out the experiments. S.J.R., M.S., C.E.E., M.K., J.J., and A.K.S. performed the analysis and helped with the interpretation. K.N. and M.S. developed the FACPACK analysis methodology. S.J.R., M.S., C.E.E., and S.W. wrote the article.

ACKNOWLEDGMENTS

We thank Gertien Smits for suggesting the slow hydrolysis reaction as an explanation for the loss of peptide bonds at long timescales.

S.J.R. acknowledges funding from the Villum 2515 Foundation (Experiment Grant 22956) and the 2516 Lundbeck Foundation for a postdoctoral fellowship.

REFERENCES

1. Pulawski, W., U. Ghoshdastider, …, S. Filipek. 2012. Ubiquitous amyloids. *Appl. Biochem. Biotechnol.* 166:1626–1643.
2. Benilova, I., E. Karran, and B. De Strooper. 2012. The toxic Aβ oligomer and Alzheimer's disease: an emperor in need of clothes. *Nat. Neurosci.* 15:349–357.
3. Baronio, C. M., M. Baldassarre, and A. Barth. 2019. Insight into the internal structure of amyloid-β oligomers by isotope-edited Fourier transform infrared spectroscopy. *Phys. Chem. Chem. Phys.* 21:8587–8597.
4. Winner, B., R. Jappelli, …, R. Riek. 2011. In vivo demonstration that alpha-synuclein oligomers are toxic. *Proc. Natl. Acad. Sci. USA.* 108:4194–4199.
5. Ono, K. 2017. The oligomer hypothesis in α-synucleinopathy. *Neurochem. Res.* 42:3362–3371.
6. Haataja, L., T. Gurlo, …, P. C. Butler. 2008. Islet amyloid in type 2 diabetes, and the toxic oligomer hypothesis. *Endocr. Rev.* 29:303–316.
7. Birol, M., S. Kumar, …, A. D. Miranker. 2018. Conformational switching within dynamic oligomers underpins toxic gain-of-function by diabetes-associated amyloid. *Nat. Commun.* 9:1312.
8. Barth, A. 2007. Infrared spectroscopy of proteins. *Biochim. Biophys. Acta.* 1767:1073–1101.
9. Hamm, P., and M. Zanni. 2011. Concepts and Methods of 2D Infrared Spectroscopy. Cambridge University Press, Cambridge, UK.
10. Strasfeld, D. B., Y. L. Ling, …, M. T. Zanni. 2008. Tracking fiber formation in human islet amyloid polypeptide with automated 2D-IR spectroscopy. *J. Am. Chem. Soc.* 130:6698–6699.
11. Shim, S.-H., R. Gupta, …, M. T. Zanni. 2009. Two-dimensional IR spectroscopy and isotope labeling defines the pathway of amyloid formation with residue-specific resolution. *Proc. Natl. Acad. Sci. USA.* 106:6614–6619.

12. Strasfeld, D. B., Y. L. Ling, …, M. T. Zanni. 2009. Strategies for extracting structural information from 2D IR spectroscopy of amyloid: application to islet amyloid polypeptide. *J. Phys. Chem. B.* 113:15679–15691.

13. Moran, S. D., S. M. Decatur, and M. T. Zanni. 2012. Structural and sequence analysis of the human γD-crystallin amyloid fibril core using 2D IR spectroscopy, segmental 13C labeling, and mass spectrometry. *J. Am. Chem. Soc.* 134:18410–18416.

14. Moran, S. D., A. M. Woys, …, M. T. Zanni. 2012. Two-dimensional IR spectroscopy and segmental 13C labeling reveals the domain structure of human γD-crystallin amyloid fibrils. *Proc. Natl. Acad. Sci. USA.* 109:3329–3334.

15. Middleton, C. T., P. Marek, …, M. T. Zanni. 2012. Two-dimensional infrared spectroscopy reveals the complex behaviour of an amyloid fibril inhibitor. *Nat. Chem.* 4:355–360.

16. Moran, S. D., T. O. Zhang, …, M. T. Zanni. 2013. Amyloid fiber formation in human γD-Crystallin induced by UV-B photodamage. *Biochemistry.* 52:6169–6181.

17. Moran, S. D., T. O. Zhang, and M. T. Zanni. 2014. An alternative structural isoform in amyloid-like aggregates formed from thermally denatured human γD-crystallin. *Protein Sci.* 23:321–331.

18. Buchanan, L. E., J. K. Carr, …, M. T. Zanni. 2014. Structural motif of polyglutamine amyloid fibrils discerned with mixed-isotope infrared spectroscopy. *Proc. Natl. Acad. Sci. USA.* 111:5796–5801.

19. Moran, S. D., and M. T. Zanni. 2014. How to get insight into amyloid structure and formation from infrared spectroscopy. *J. Phys. Chem. Lett.* 5:1984–1993.

20. Lomont, J. P., J. S. Ostrander, …, M. T. Zanni. 2017. Not all β-sheets are the same: amyloid infrared spectra, transition dipole strengths, and couplings investigated by 2D IR spectroscopy. *J. Phys. Chem. B.* 121:8935–8945.

21. Iyer, A., S. J. Roeters, …, V. Subramaniam. 2016. The impact of N-terminal acetylation of α-synuclein on phospholipid membrane binding and fibril structure. *J. Biol. Chem.* 291:21110–21122.

22. Iyer, A., S. J. Roeters, …, V. Subramaniam. 2017. C-Terminal truncated α-synuclein fibrils contain strongly twisted β-sheets. *J. Am. Chem. Soc.* 139:15392–15400.

23. Roeters, S. J., A. Iyer, …, S. Woutersen. 2017. Evidence for intramolecular antiparallel beta-sheet structure in alpha-synuclein fibrils from a combination of two-dimensional infrared spectroscopy and atomic force microscopy. *Sci. Rep.* 7:41051.

24. Ling, Y. L., D. B. Strasfeld, …, M. T. Zanni. 2009. Two-dimensional infrared spectroscopy provides evidence of an intermediate in the membrane-catalyzed assembly of diabetic amyloid. *J. Phys. Chem. B.* 113:2498–2505.

25. Buchanan, L. E., E. B. Dunkelberger, …, M. T. Zanni. 2013. Mechanism of IAPP amyloid fibril formation involves an intermediate with a transient β-sheet. *Proc. Natl. Acad. Sci. USA.* 110:19285–19290.

26. Ma, S., X. Cao, …, L. A. Nafie. 2007. Vibrational circular dichroism shows unusual sensitivity to protein fibril formation and development in solution. *J. Am. Chem. Soc.* 129:12364–12365.

27. Nafie, L. A. 2011. Vibrational Optical Activity: Principles and Applications. John Wiley & Sons, Ltd, Chichester, UK.

28. Kurouski, D., R. K. Dukor, …, I. K. Lednev. 2012. Normal and reversed supramolecular chirality of insulin fibrils probed by vibrational circular dichroism at the protofilament level of fibril structure. *Biophys. J.* 103:522–531.

29. Kurouski, D., X. Lu, …, L. A. Nafie. 2014. Is supramolecular filament chirality the underlying cause of major morphology differences in amyloid fibrils? *J. Am. Chem. Soc.* 136:2302–2312.

30. Ivanova, M. I., M. J. Thompson, and D. Eisenberg. 2006. A systematic screen of beta(2)-microglobulin and insulin for amyloid-like segments. *Proc. Natl. Acad. Sci. USA.* 103:4079–4082.

31. Gibson, T. J., and R. M. Murphy. 2006. Inhibition of insulin fibrillogenesis with targeted peptides. *Protein Sci.* 15:1133–1141.

32. Sawaya, M. R., S. Sambashivan, …, D. Eisenberg. 2007. Atomic structures of amyloid cross-beta spines reveal varied steric zippers. *Nature.* 447:453–457.

33. Seo, J., W. Hoffmann, …, K. Pagel. 2017. An infrared spectroscopy approach to follow β-sheet formation in peptide amyloid assemblies. *Nat. Chem.* 9:39–44.

34. Matthes, D., V. Daebel, …, B. L. de Groot. 2014. Spontaneous aggregation of the insulin-derived steric zipper peptide VEALYL results in different aggregation forms with common features. *J. Mol. Biol.* 426:362–376.

35. Huerta-Viga, A., D. J. Shaw, and S. Woutersen. 2010. pH dependence of the conformation of small peptides investigated with two-dimensional vibrational spectroscopy. *J. Phys. Chem. B.* 114:15212–15220.

36. Helbing, J., and P. Hamm. 2011. Compact implementation of Fourier transform two-dimensional IR spectroscopy without phase ambiguity. *J. Opt. Soc. Am. B.* 28:171–178.

37. Arosio, P., T. P. J. Knowles, and S. Linse. 2015. On the lag phase in amyloid fibril formation. *Phys. Chem. Chem. Phys.* 17:7606–7618.

38. Nielsen, L., R. Khurana, …, A. L. Fink. 2001. Effect of environmental factors on the kinetics of insulin fibril formation: elucidation of the molecular mechanism. *Biochemistry.* 40:6036–6046.

39. Uversky, V. N. 2003. A protein-chameleon: conformational plasticity of alpha-synuclein, a disordered protein involved in neurodegenerative disorders. *J. Biomol. Struct. Dyn.* 21:211–234.

40. Cohen, S. I. A., S. Linse, …, T. P. J. Knowles. 2013. Proliferation of amyloid-β42 aggregates occurs through a secondary nucleation mechanism. *Proc. Natl. Acad. Sci. USA.* 110:9758–9763.

41. Buell, A. K., C. Galvagnion, …, C. M. Dobson. 2014. Solution conditions determine the relative importance of nucleation and growth processes in α-synuclein aggregation. *Proc. Natl. Acad. Sci. USA.* 111:7671–7676.

42. Zandomeneghi, G., M. R. Krebs, …, M. Fändrich. 2004. FTIR reveals structural differences between native β-sheet proteins and amyloid fibrils. *Protein Sci.* 13:3314–3321.

43. Dioumaev, A. K., and M. S. Braiman. 1995. Modeling vibrational spectra of amino acid side chains in proteins: the carbonyl stretch frequency of buried carboxylic residues. *J. Am. Chem. Soc.* 117:10572–10574.

44. Golub, G., and C. Van Loan. 2012. Matrix Computations. Johns Hopkins Studies in the Mathematical Sciences. Johns Hopkins University Press, Baltimore, MD.

45. Lawton, W. H., and E. A. Sylvestre. 1971. Self modeling curve resolution. *Technometrics.* 13:617630.

46. Sawall, M., and K. Neymeyr. 2014. 6. How to compute the area of feasible solutions, a practical study and users' guide to FACPACK. *In* Current Applications of Chemometrics. M. Khanmohammadi, ed. Nova Science Publishers, pp. 97–134.

47. Sawall, M., A. Jürß, and K. Neymeyr. 2015. FACPACK: a software for the computation of multi-component factorizations and the area of feasible solutions, revision 1.3. *In* FACPACK homepage http://www.math.uni-rostock.de/facpack/.

48. Borgen, O., and B. Kowalski. 1985. An extension of the multivariate component-resolution method to three components. *Anal. Chim. Acta.* 174:1–26.

49. Rajkó, R., and K. István. 2005. Analytical solution for determining feasible regions of self-modeling curve resolution (SMCR) method based on computational geometry. *J. Chemometr.* 19:448–463.

50. Sawall, M., C. Kubis, …, K. Neymeyr. 2013. A fast polygon inflation algorithm to compute the area of feasible solutions for three-component systems. I: concepts and applications. *J. Chemometr.* 27:106–116.

51. Sawall, M., and K. Neymeyr. 2014. A fast polygon inflation algorithm to compute the area of feasible solutions for three-component systems. II: Theoretical foundation, inverse polygon inflation, and FACPACK implementation. *J. Chemometr.* 28:633–644.

52. Golshan, A., H. Abdollahi, …, R. Tauler. 2016. A review of recent methods for the determination of ranges of feasible solutions resulting

from soft modelling analyses of multivariate data. *Anal. Chim. Acta.* 911:1–13.

53. Sawall, M., A. Jürß, …, K. Neymeyr. 2016. 5. On the analysis and computation of the area of feasible solutions for two-, three- and four-component systems. *In* Resolving Spectral Mixtures With Applications from Ultrafast Time-Resolved Spectroscopy to Super-Resolution Imaging. C. Ruckebusch, ed. Elsevier, pp. 135–184.
54. Honig, B. H., and W. L. Hubbell. 1984. Stability of "salt bridges" in membrane proteins. *Proc. Natl. Acad. Sci. USA.* 81:5412–5416.
55. Fersht, A. 1999. Structure and Mechanism in Protein Science: A Guide to Enzyme Catalysis and Protein Folding. W. H. Freeman, New York.
56. Kowalski, B. R., and M. B. Seasholtz. 1991. Recent developments in multivariate calibration. *J. Chemometr.* 5:129–145.
57. Tauler, R., B. Kowalski, and S. Fleming. 1993. Multivariate curve resolution applied to spectral data from multiple runs of an industrial process. *Anal. Chem.* 65:2040–2047.
58. Jaumot, J., A. de Juan, and R. Tauler. 2015. MCR-ALS GUI 2.0: new features and applications. *Chemom. Intell. Lab. Syst.* 140:1–12.
59. Ganim, Z., H. S. Chung, …, A. Tokmakoff. 2008. Amide I two-dimensional infrared spectroscopy of proteins. *Acc. Chem. Res.* 41:432–441.
60. Demirdöven, N., C. M. Cheatum, …, A. Tokmakoff. 2004. Two-dimensional infrared spectroscopy of antiparallel beta-sheet secondary structure. *J. Am. Chem. Soc.* 126:7981–7990.
61. Grechko, M., and M. T. Zanni. 2012. Quantification of transition dipole strengths using 1D and 2D spectroscopy for the identification of molecular structures via exciton delocalization: application to α-helices. *J. Chem. Phys.* 137:184202.
62. Siegman, A. E. 1986. Lasers. University Science Books, Sausalito, CA.
63. Salamatova, E., A. V. Cunha, …, M. S. Pshenichnikov. 2018. Hydrophobic collapse in N-methylacetamide-water mixtures. *J. Phys. Chem. A.* 122:2468–2478.
64. Cunha, A. V., E. Salamatova, …, T. L. C. Jansen. 2017. Interplay between hydrogen bonding and vibrational coupling in liquid N-methylacetamide. *J. Phys. Chem. Lett.* 8:2438–2444.
65. Levine, I. N. 1975. Molecular Spectroscopy. Wiley, New York.
66. Nafie, L. A., and T. B. Freedman. 1983. Vibronic coupling theory of infrared vibrational transitions. *J. Chem. Phys.* 78:7108–7116.
67. Kurouski, D., J. Washington, …, I. K. Lednev. 2012. Disulfide bridges remain intact while native insulin converts into amyloid fibrils. *PLoS One.* 7:e36989.
68. Choi, J. H., B. C. May, …, F. E. Cohen. 2009. Molecular modeling of the misfolded insulin subunit and amyloid fibril. *Biophys. J.* 97:3187–3195.
69. Bassett, D. C. 2003. Polymer spherulites: a modern assessment. *J. Polym. Sci. B.* 42:227–256.
70. Krebs, M. R., C. E. Macphee, …, A. M. Donald. 2004. The formation of spherulites by amyloid fibrils of bovine insulin. *Proc. Natl. Acad. Sci. USA.* 101:14420–14424.
71. Measey, T. J., and R. Schweitzer-Stenner. 2011. Vibrational circular dichroism as a probe of fibrillogenesis: the origin of the anomalous intensity enhancement of amyloid-like fibrils. *J. Am. Chem. Soc.* 133:1066–1076.
72. Marty, R., H. Frauenrath, and J. Helbing. 2014. Aggregates from perylene bisimide oligopeptides as a test case for giant vibrational circular dichroism. *J. Phys. Chem. B.* 118:11152–11160.
73. Avrami, M. 1939. Kinetics of phase change. I. General theory. *J. Chem. Phys.* 7:1103–1112.
74. Avrami, M. 1940. Kinetics of phase change. II transformation-time relations for random distribution of nuclei. *J. Chem. Phys.* 8:212–224.
75. Avrami, M. 1941. Granulation, phase change, and microstructure kinetics of phase change: III. *J. Chem. Phys.* 9:177–184.
76. Price, F. P. 1965. Some comments on the "Avrami" equation. *J. Appl. Phys.* 36:3014–3016.
77. Jena, A., and M. Chaturvedi. 1992. Phase Transformation in Materials. Prentice Hall, Englewood Cliffs, NJ.
78. Lorenzo, A. T., M. L. Arnal, …, A. J. Müller. 2007. DSC isothermal polymer crystallization kinetics measurements and the use of the Avrami equation to fit the data: guidelines to avoid common problems. *Polym. Test.* 26:222–231.
79. Smilde, A., R. Bro, and P. Geladi. 2004. Multi-Way Analysis: Applications in the Chemical Sciences. John Wiley & Sons, Inc, New York.